JOURNAL OF AIRCRAFT
Vol. 29, No. 6, Nov.–Dec. 1992

Numerical Simulation of Re-Entry Flow Around the Space Shuttle with Finite-Rate Chemistry

Yasuhiro Wada*
National Aerospace Laboratory, Tokyo 182, Japan
and
Hirotoshi Kubota†
University of Tokyo, Tokyo 113, Japan

Hypersonic flow around the Space Shuttle is computed for a series of re-entry flight conditions by incorporating a one-temperature model that takes into account 7-species finite-rate chemistry. An implicit higher-order upwind scheme based on a generalized Roe's approximate Riemann is used. The aerodynamic characteristics and heating rates are compared with the STS-2 flight data, and good agreement is obtained. These results quantitatively confirm the measured forward shift of the center of pressure and reduction of heating rates caused by real gas effects.

Introduction

In recent years, increased interest has been focused on hypersonic aerodynamics due to newly proposed aerospace development plans such as space-planes (SP) and aero-assisted orbital transfer vehicles (AOTV). Since no ground-based experimental facilities can completely duplicate these flight conditions, computational fluid dynamics (CFD) is considered to be a primary technique for estimating the aerodynamic characteristics and heating rates. Space Shuttle flights are unique because they offer repeated opportunities to conduct aerodynamic and aerothermodynamic research related to a full-scale winged vehicle moving through a real environment at hypersonic speed. The Space Shuttle has provided very valuable data for supporting ongoing research related to the future space transportation system. The Space Shuttle flights indicate that the trim characteristics have not been accurately predicted by wind-tunnel experiments.[1] Maus et al.[2] applied a CFD code to investigate the differences between aerodynamic predictions and data from STS-1 flight (the first Space Shuttle flight), with results indicating that the differences are primarily due to real-gas effects. However, a modified Space Shuttle orbiter geometry was incorporated for simplicity, and the calculated gas model was inviscid, and in chemical equilibrium, thereby being unable to either duplicate the viscous effects on aerodynamic forces or to analyze aerodynamic heating.

Robust and high-resolution schemes should be used to investigate hypersonic flows because of the resulting strong discontinuities, and several modern shock-capturing methods have been devised,[3,4] making use of exact or approximate solution of the Riemann problem,[5] and achieving higher-order accuracy and numerical stability under the restriction of a total variation diminishing (TVD) condition.[6] In these numerical methods, eigenvalues and the corresponding eigenvectors of flux Jacobian matrices play an important role, and those of nonequilibrium real gas-dynamic equations are presented in Refs. 7–9. In Ref. 9 especially, the governing equations include total mass conservation, and arbitrary nonequilibrium effects are treated in the same fashion. Efforts to extend Roe's approximate Riemann solver to real gases have recently been reported.[10,11]

This led to the present study, which computes the hypersonic flow around the Space Shuttle for a series of re-entry flight conditions, using both perfect- and real-gas models. In the real-gas computation, a one-temperature model is assumed that takes into account the finite-rate chemistry of 7-species. An implicit higher-order upwind scheme based on a generalized Roe's approximate Riemann solver is then used. This numerical code has been validated in Ref. 12. The computed aerodynamic characteristics and heating rates are compared to STS-2 flight data.[13,14]

Governing Equations

Three-dimensional Navier-Stokes equations incorporating nonequilibrium effects are generally given in a conservative form

$$\frac{\partial \boldsymbol{q}}{\partial t} + \frac{\partial \boldsymbol{F}_k}{\partial x_k} + \frac{\partial \boldsymbol{F}\boldsymbol{v}_k}{\partial x_k} = \boldsymbol{S} \tag{1}$$

where

$$\boldsymbol{q} = \begin{bmatrix} \rho \\ \rho u_1 \\ \rho u_2 \\ \rho u_3 \\ E \\ f_1 \\ f_2 \\ \vdots \\ f_n \end{bmatrix}, \quad \boldsymbol{F}_k = \begin{bmatrix} \rho u_k \\ \rho u_1 u_k + \delta_{1,k} p \\ \rho u_2 u_k + \delta_{2,k} p \\ \rho u_3 u_k + \delta_{3,k} p \\ (E + p) u_k \\ f_1 u_k \\ f_2 u_k \\ \vdots \\ f_n u_k \end{bmatrix}, \quad \boldsymbol{S} = \begin{bmatrix} 0 \\ 0 \\ 0 \\ 0 \\ 0 \\ s_1 \\ s_2 \\ \vdots \\ s_n \end{bmatrix}$$

$$E = e + \tfrac{1}{2}\rho(u_1^2 + u_2^2 + u_3^3)$$

$$p = p(\rho, e, f_1, f_2, \ldots, f_n)$$

These equations include the conservation of total mass, momentum, total energy, and also the physical quantities f_i which represent nonequilibrium effects, i.e., either the concentration of each chemical species or vibrational energy. The quantities p, ρ, u_k, E, and e, respectively denote the pressure, density, Cartesian velocity components, total, and internal energies; whereas the vectors $\boldsymbol{F}$ and $\boldsymbol{Fv}$ are the convective and viscous flux, and the vector $\boldsymbol{S}$ is a set of elements of nonequilibrium source terms. The Eq. (1) system can be trans-

Received Aug. 6, 1991; revision received Oct. 18, 1991; accepted for publication Oct. 18, 1991.

*Research Scientist, Computational Sciences Division, 7-44-1 Jindaijihigashi-machi Chofu-shi.
†Professor, Department of Aeronautics, 7-3-1 Hongo Bunkyo-ku. Associate Fellow AIAA.

formed into generalized curvilinear coordinates $(\tau, \xi_1, \xi_2, \xi_3)$

$$\frac{\partial \hat{q}}{\partial \tau} + \frac{\partial \hat{F}_k}{\partial \xi_k} + \frac{\partial \hat{Fv}_k}{\partial \xi_k} = \hat{S} \tag{2}$$

with

$$\hat{q} = Vq, \quad \hat{F}_k = n_{1k}F_1 + n_{2k}F_2 + n_3kF_3$$

$$\hat{Fv}_k = n_{1k}Fv_1 + n_{2k}Fv_2 + n_{3k}Fv_3$$

$$\hat{S} = VS$$

where V is the volume of a computational cell around a grid point, and vectors $n_k(n_{1k}, n_{2k}, n_{3k})$ are cell-interface normals for the ξ_k-direction.

A one-temperature model, that assumes thermal equilibrium, is used in the present study, with the rotational, vibrational, and electronic excitation energies being considered to be in equilibrium with the translational energy. This assumption is valid for hypersonic flow at relatively low altitudes. The internal energy e is then given as

$$e = \sum_s \rho z_s \left(\int Cp_s \, dT + \Delta H_{fs} \right) - p \tag{3}$$

where z_s is mole number density per unit mass of species s (Kmole/kg), with ΔH_{fs} and Cp_s being the heat of formation and specific heat at constant pressure.[15] The equation for conserving the number of each chemical species is represented by considering the quantities f_i in the additional Eq. (1) equations as ρz_i. The following chemical reaction model which includes 7-species is used[16]:

1) $O_2 + M \rightleftarrows O + O + M$, M=N, NO, O, O_2, N_2

2) $N_2 + M \rightleftarrows N + N + M$, M=N, NO, O, O_2, N_2

3) $NO + M \rightleftarrows N + O + M$, M=N, NO, O, O_2, N_2

4) $O + NO \rightleftarrows N + O_2$

5) $O + N_2 \rightleftarrows N + NO$

6) $O + N \rightleftarrows NO^+ + e^-$

The thin-layer Navier-Stokes approximation is assumed by dropping the ξ_1- and ξ_2-direction derivatives in the viscous terms. The viscous flux vector $\hat{Fv}_3$ in Eq. (2) is given as

$$\hat{Fv}_3 = \frac{1}{V} \begin{bmatrix} 0 \\ \mu n^2 u_{1\xi_3} + (\mu/3) n_1 (n_1 u_{1\xi_3} + n_2 u_{2\xi_3} + n_3 u_{3\xi_3}) \\ \mu n^2 u_{2\xi_3} + (\mu/3) n_2 (n_1 u_{1\xi_3} + n_2 u_{2\xi_3} + n_3 u_{3\xi_3}) \\ \mu n^2 u_{3\xi_3} + (\mu/3) n_3 (n_1 u_{1\xi_3} + n_2 u_{2\xi_3} + n_3 u_{3\xi_3}) \\ \frac{1}{2}\mu(u_1^2 + u_2^2 + u_3^2) + (\mu/3)(n_1 u_1 + n_2 u_2 + n_3 u_3)(n_1 u_{1\xi_3} + n_2 u_{2\xi_3} + n_3 u_{3\xi_3}) + \kappa T_{\xi_3} + \Sigma \rho D_i h_i X_{i\xi_3} \\ \rho D_1 X_{1\xi_3} \\ \rho D_2 X_{2\xi_3} \\ \vdots \\ \rho D_{ns} X_{ns\xi_3} \end{bmatrix} \tag{4}$$

where D_s is diffusion coefficient and X_s is molar fraction of species s

$$X_s = z_s \Big/ \sum_i z_i$$

The data for viscosity coefficient μ_i is taken from Ref. 16. The total viscosity μ and conductivity κ of the gas are calculated using Wilke's empirical mixing rule[17]

$$\mu = \sum_s \frac{X_s \mu_s}{\phi_s}$$

$$\kappa = \sum_s \frac{X_s \kappa_s}{\phi_s}$$

where

$$\phi_s = \sum_i X_i \left[1 + \sqrt{\frac{\mu_s}{\mu_i}} \left(\frac{M_i}{M_s} \right)^{1/4} \right]^2 \left[\sqrt{8} \sqrt{1 + \frac{M_s}{M_i}} \right]^{-1}$$

$$\kappa_s = \mu R \left(\frac{Cp_s}{R} + \frac{5}{4} \right) \sum_i z_i$$

The expression for each species diffusion coefficient is taken from Lee[18] and given by

$$D_s = \sum_i z_i (1 - z_s M_s)[1/(1 - X_s)]D$$

where the diffusion coefficient D is simply obtained if the binary Schmidt numbers Sc for all of the species are assumed to be the same (0.5)[19]

$$D = (\mu / S_c \rho)$$

This assumption is considered valid since the molecular weights of the species considered do not greatly differ.

The total mass conservation equation, and each chemical species conservation equation, are simultaneously solved so that the formulation has a redundant equation. This redundancy is retained because if one of the species variables is expressed as a combination of others, the numerical errors acquired in each computing step, by each species variable, will compound on this value.[20] However, this redundancy may also result in a discrepancy in which the sum of all species concentrations does not satisfy the overall mass conservation, due to numerical errors. This was prevented by multiplying each species concentration value by the same factor, thereby satisfying the total mass conservation solution that is free from linearization errors in the implicit treatment of stiff chemical source terms.

Numerical Method

Space Discretization

Upstream differencing schemes have been successfully used in flow computation, with Roe's approximate Riemann solver[5] being one of the most promising methods, due to its computational efficiency, and capability to achieve high resolution for stationary discontinuities. This method's numerical flux is given as

$$F(q_L, q_R) = \tfrac{1}{2}[F_L + F_R - |\tilde{P}(q_L, q_R)|\Delta q] \tag{5}$$

where $\tilde{P}(q_L, q_R)$ is the flux Jacobian matrix $P \equiv (\partial F / \partial q)$ at an average state satisfying the property U.[5] The matrix P, in generalized coordinates, is a linear combination of those in Cartesian coordinates, and the matrix $|P|$ is calculated by the use of the eigensystem decomposition

$$|P| = \left| n_t I + \sum_k n_k \frac{\partial F_k}{\partial q} \right| = T|\Lambda|T^{-1} \tag{6}$$

where T^{-1} and T are, respectively, the left and right eigenvector matrices. The diagonal matrixes of eigenvalues Λ are

easily found to be

$$\Lambda = \mathrm{diag}(U, U, U, U + |\boldsymbol{n}|c, U - |\boldsymbol{n}|c, U, U, \ldots, U) \tag{7}$$

where

$$U = n_t + n_1u_1 + n_2u_2 + n_3u_3, \quad |\boldsymbol{n}| = \sqrt{n_1^2 + n_2^2 + n_3^2}$$

$$c^2 = \frac{\partial p}{\partial \rho} + \frac{h}{\rho}\frac{\partial p}{\partial e} + \sum_i \frac{f_i}{\rho}\frac{\partial p}{\partial f_i}, \quad h = e + p$$

The eigenvectors used in the present study, are calculated using reciprocal vectors $\bar{\boldsymbol{l}}$, and $\bar{\boldsymbol{m}}$ of the normalized normal vector $\bar{\boldsymbol{n}} = (n_1, n_2, n_3)/|\boldsymbol{n}|$ for a simple expression. In actual computations, the multiplication of some vectors $\boldsymbol{\Psi}$ with the matrices of either $\boldsymbol{T}$, or $\boldsymbol{T}^{-1}$ is required with the results being presented as follows:

1) $\boldsymbol{T}^{-1}\boldsymbol{\Psi}$

$$\boldsymbol{T}^{-1}\begin{bmatrix}\psi_1\\ \psi_2\\ \psi_3\\ \psi_4\\ \psi_5\\ \psi_6\\ \psi_7\\ \vdots\\ \psi_{5+n}\end{bmatrix} = \begin{bmatrix} c^2\psi_1 - aa \\ -(\bar{\boldsymbol{l}}\cdot\boldsymbol{u})c\psi_1 + c(\bar{l}_1\psi_2 + \bar{l}_2\psi_3 + \bar{l}_3\psi_4) \\ -(\bar{\boldsymbol{m}}\cdot\boldsymbol{u})c\psi_1 + c(\bar{m}_1\psi_2 + \bar{m}_2\psi_3 + \bar{m}_3\psi_4) \\ (aa + bb)/2 \\ (aa - bb)/2 \\ -(f_1/\rho)aa + c^2\psi_6 \\ -(f_2/\rho)aa + c^2\psi_7 \\ \vdots \\ -(f_n/\rho)aa + c^2\psi_{5+n} \end{bmatrix} \tag{8}$$

where

$$aa \equiv \left(\frac{\partial p}{\partial e}\frac{u^2}{2} + \frac{\partial p}{\partial \rho}\right)\psi_1 - \frac{\partial p}{\partial e}(u_1\psi_2 + u_2\psi_3 + u_3\psi_4 - \psi_5) + \sum_i \frac{\partial p}{\partial f_i}\psi_{5+i}$$

$$bb \equiv c[-(\bar{\boldsymbol{n}}\cdot\mathbf{u})\psi_1 + \bar{n}_1\psi_2 + \bar{n}_2\psi_3 + \bar{n}_3\psi_4]$$

2) $\boldsymbol{T}\boldsymbol{\Psi}$

$$\boldsymbol{T}\begin{bmatrix}\psi_1\\ \psi_2\\ \psi_3\\ \psi_4\\ \psi_5\\ \psi_6\\ \psi_7\\ \vdots\\ \psi_{5+n}\end{bmatrix} = \begin{bmatrix} \frac{1}{c^2}[\psi_1 + \psi_4 + \psi_5] \\ \frac{u_1}{c^2}[\psi_1 + \psi_4 + \psi_4] + \frac{1}{c}[\bar{l}_1\psi_2 + \bar{m}_1\psi_3 + \bar{n}_1(\psi_4 - \psi_5)] \\ \frac{u_2}{c^2}[\psi_1 + \psi_4 + \psi_5] + \frac{1}{c}[\bar{l}_2\psi_2 + \bar{m}_2\psi_3 + \bar{n}_2(\psi_4 - \psi_5)] \\ \frac{u_3}{c^2}[\psi_1 + \psi_4 + \psi_5] + \frac{1}{c}[\bar{l}_3\psi_2 + \bar{m}_3\psi_3 + \bar{n}_3(\psi_4 - \psi_5)] \\ \left\{\frac{u^2}{2} - \frac{\frac{\partial p}{\partial \rho}}{\frac{\partial p}{\partial e}}\right\}\frac{\psi_1}{c^2} + \frac{1}{c}[(\boldsymbol{u}\cdot\bar{\boldsymbol{l}})\psi_2 + (\boldsymbol{u}\cdot\bar{\boldsymbol{m}})\psi_3 + (\boldsymbol{u}\cdot\bar{\boldsymbol{n}})(\psi_4 - \psi_5)] + \frac{1}{c^2}\left(\frac{u^2}{2} + \frac{h}{\rho}\right)(\psi_4 + \psi_5) - \sum_i \frac{\frac{\partial p}{\partial f_i}}{\frac{\partial p}{\partial e}}\frac{\psi_{5+i}}{c^2} \\ \frac{f_1}{\rho c^2}(\psi_4 + \psi_5) + \frac{1}{c^2}\psi_6 \\ \frac{f_2}{\rho c^2}(\psi_4 + \psi_5) + \frac{1}{c^2}\psi_7 \\ \vdots \\ \frac{f_n}{\rho c^2}(\psi_4 + \psi_5) + \frac{1}{c^2}\psi_{5+n} \end{bmatrix} \tag{9}$$

The Roe average state for the nonequilibrium gas Eqs. (2) is determined using Ref. 11. When $\boldsymbol{T}^{-1}$ is in a Roe-average state, a simple form for the characteristic vector $\bar{\boldsymbol{T}}^{-1}\Delta\boldsymbol{q}$ is given as

$$\bar{\boldsymbol{T}}^{-1}\Delta\boldsymbol{q} = \begin{bmatrix} \bar{c}^2\Delta\rho - \Delta p \\ \bar{\rho}\bar{c}(\bar{\boldsymbol{l}}\cdot\Delta\boldsymbol{u}) \\ \bar{\rho}\bar{c}(\bar{\boldsymbol{m}}\cdot\Delta\boldsymbol{u}) \\ [\Delta p + \bar{\rho}\bar{c}(\bar{\boldsymbol{n}}\cdot\Delta\boldsymbol{u})]/2 \\ [\Delta p - \bar{\rho}\bar{c}(\bar{\boldsymbol{n}}\cdot\Delta\boldsymbol{u})]/2 \\ \bar{c}^2\Delta f_1 - (\bar{f}_1/\bar{\rho})\Delta p \\ \bar{c}^2\Delta f_2 - (\bar{f}_2/\bar{\rho}\Delta p \\ \vdots \\ \bar{c}^2\Delta f_n - (\bar{f}_n/\bar{\rho})\Delta p \end{bmatrix} \tag{10}$$

Roe's approximate Riemann solver[5] is a first-order scheme, therefore, to extend this method to a higher order one, the Chakravarthy-Oshers' post-processing fully upwind second-order TVD scheme[3] is used. This method is more efficient than using the monotonic upstream-centered scheme for conservation laws (MUSCL) for real-gas flow problems, since the latter method needs the temperature value at each cell interface and, therefore, requires Newton iterations. The presented scheme slightly differs from the original one, i.e., characteristic variables are extrapolated instead of fluxes,[9,21] the eigenvectors of the gas-dynamic matrices are chosen so that $\bar{\boldsymbol{T}}^{-1}\Delta\boldsymbol{q}$ has the unit of the pressure,[22] and an artificial viscosity is added on linear waves, as well as the entropy fixing viscosity on the nonlinear wave at a sonic point of a rarefaction fan. The original scheme fails at extremely strong shock waves, thus, the first modification is necessary to enable hypersonic calculations. The second modification ensures rapid convergence, whereas, the third one is needed to remove the instability near the stagnation region in hypersonic computations.[23] This additional viscosity, however, is not added in the direction normal to the wall to accurately evaluate heating rates. Klopfer et al.[24] presented hypersonic flow calculations around a cylinder, and reported that the cell Reynolds number should be on the order of unity when computing heat transfer results. However, they employed the artificial viscosity on every wave,[25] which degrades the numerical accuracy for heating rates. Figure 1 shows the calculated heating rates at the cylinder stagnation ($M = 8.03$, $Re/D = 1.86 \times 10^5$) using Klopfer's artificial viscosity and the present one, with varying amounts of mesh clustering at the wall. Although both computed values are correlated with the Detra-Kemp-Riddell's formula[26] near the cell Reynolds number of unity, it is obvious that this

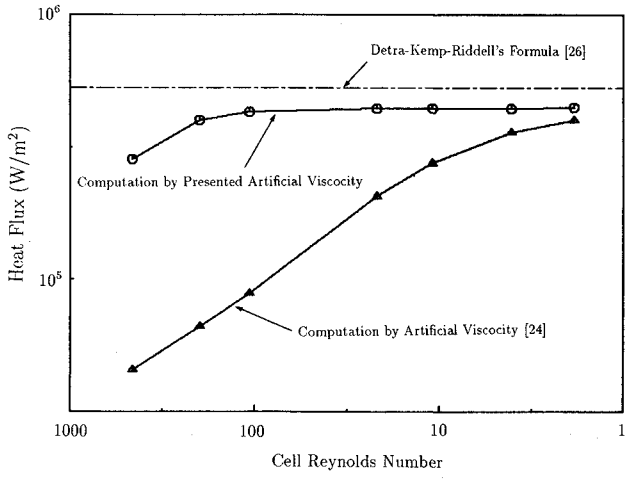

Fig. 1 Blunt body stagnation heat flux as a function of cell Reynolds number.

artificial viscosity makes the cell Reynolds number on the order of 100 to be sufficient for computing heating rates, whereas Klopfer's method requires an even finer grid.

Time-Integration Method

Nonequilibrium flows include several characteristic time scales at a specific time and location—those of fluid and chemical reactions. Such a disparity in time scales is referred to as "stiffness," causing numerical instability in time-marching procedures, and being one of the main obstacles in nonequilibrium flow computations. Thus, each term in the governing equations, especially chemical source ones, should be implicitly treated to construct stable numerical schemes. In perfect gas calculations, the alternative direction implicit (ADI) scheme is one of the most popular methods. However, the ADI method requires the inversion of a block tri-diagonal matrix, becoming complex as the length of the dependent variable vector $\boldsymbol{n}$ is cubed, thus making this scheme too time-consuming for nonequilibrium flow computations.

In the present study, an implicit scheme is used. The implicit operator is factored into convective and chemical source terms, with each convective block operator being diagonalized so that the block matrix operation is reduced to scalar operations. The implicit operator for the viscous terms is approximately included in convective operators to enhance numerical stability, and local time-stepping is also incorporated in order to accelerate convergence. Implicit schemes, however, are sometimes less stable than explicit ones at extremely strong shock waves, due to the strong nonlinearity of the governing equations, hence, only the chemical source terms are implicitly treated near shock waves, with the rest being explicitly handled. This method is easily constructed by replacing the tri-diagonal scalar operators by a unit matrix, and since the detection of shock waves is initially required to prevent unphysical expansion shocks, no additional calculations are needed. This implicit time integration method is expressed as

$$\boldsymbol{LHS}\Delta\boldsymbol{q} = -\Delta t\,(\hat{\boldsymbol{F}}_{1_{j+1/2}} - \hat{\boldsymbol{F}}_{1_{j-1/2}} + \hat{\boldsymbol{F}}_{2_{k+1/2}} - \hat{\boldsymbol{F}}_{2_{k-1/2}} + \hat{\boldsymbol{F}}_{3_{l+1/2}} - \hat{\boldsymbol{F}}_{3_{l-1/2}} + \hat{\boldsymbol{F}}\hat{\boldsymbol{v}}_{3_{l+1/2}} - \hat{\boldsymbol{F}}\hat{\boldsymbol{v}}_{3_{l-1/2}} - \boldsymbol{VS})/V \tag{11}$$

$$\boldsymbol{q}^{n+1} = \boldsymbol{q}^{n} + \Delta\boldsymbol{q} \tag{12}$$

with $\hat{\boldsymbol{F}}_1$, $\hat{\boldsymbol{F}}_2$, and $\hat{\boldsymbol{F}}_3$ being the TVD numerical fluxes. The $\boldsymbol{LHS}$ is an implicit operator that is given as

$$\boldsymbol{LHS} = (\boldsymbol{I} - \Delta t\boldsymbol{H})\boldsymbol{T}_{\xi 1}[\boldsymbol{I} + (\Delta t/V)\delta_{\xi 1}\boldsymbol{\Lambda}]\boldsymbol{T}_{\xi 1}^{-1}\boldsymbol{T}_{\xi 2} \cdot [\boldsymbol{I} + (\Delta t/V)\delta_{\xi 2}\boldsymbol{\Lambda}]\boldsymbol{T}_{\xi 2}^{-1}\boldsymbol{T}_{\xi 3}[\boldsymbol{I} + \frac{\Delta t}{V}(\delta_{\xi 3}\boldsymbol{\Lambda} - \boldsymbol{D}_{\mu})]\boldsymbol{T}_{\xi 3}^{-1}, \tag{13}$$

where the differential operator δ consists of backward Δ, and forward differences ∇

$$\delta\boldsymbol{\Lambda} = \begin{cases} \boldsymbol{0} & \text{at shock wave} \\ \Delta\boldsymbol{\Lambda}^{+} + \nabla\boldsymbol{\Lambda}^{-} & \text{otherwise} \end{cases}$$

$$\boldsymbol{D}_{\mu} = (\kappa/CvV)n_3^2$$

$$\boldsymbol{H} \equiv (\partial\boldsymbol{S}/\partial\boldsymbol{q})$$

Numerical Results

Re-entry flow around the Space Shuttle has been calculated and compared with the flight data from the Space Shuttle's second flight (STS-2).[13,14] Selected flight Mach numbers range from 7.0–26.0, with these conditions given in Table 1. The wall is assumed to be noncatalytic at a constant temperature (1200 K) and in a no-slip condition. Figure 2 shows an algebraically generated computational grid system[27]: consisting of 86 points in the chord-wise direction, 69 points in the circumferential direction, and 66 points from the body to the outer boundary, with the cell Reynolds number near the wall being taken to be on the order of 10 for each computation. An adaptive grid technique is applied to clearly capture the bow shock wave.[21] This procedure, however, has almost no influence on the evaluation of the heat flux and aerodynamic characteristics. The Space Shuttle configuration is read from Refs. 28 and 29 using a dram-scanner, and several numerical techniques such as smoothing are applied, thus, the generated surface data may not exactly coincide with the original shape. Each converged real-gas solution is obtained with the residual reduction of three-order magnitude after ≈5000 iterations using 23 μ/s for each time step and grid point, with the total CPU time being ≈12 h using the Fujitsu VP-400 supercomputer at the National Aerospace Laboratory. Figure 3a shows real-gas pressure distributions (M_∞ = 15.7), with the two-dimensional particle path traces and pressure distributions on a cross-sectional plane (X/L = 50%) presented in Fig. 3b. The windward shock layer is very thin due to the angle of attack (42 deg), and the flowfield structure can be seen, i.e., expansion fans around the wing tip and body shoulder, an oblique shock wave over the recirculation region above the cargo bay, a weak bow shock wave over the side body and engine pods, and also a streak vortex. Limiting streamline patterns are presented in Fig. 4 where the separation and reattachment phenomena are clarified. Comparison of the pressure distributions between real and perfect gases on a cross-sectional plane at X/L = 0.8 are shown in Figs. 5a–c for respective Mach numbers of 11.9, 15.7, and 26.3, where the real-gas shock layer is observed to be thinner than that of the perfect-gas.

Figure 6 shows the dissociated oxygen atom mole fraction distributions (M_∞ = 15.7), where the oxygen atoms that dissociate near the nose region, are carried over to the leeward side, and concentrate on the symmetric plane. The oxygen

Table 1 Selected flight conditions for STS-2

	Case 1	Case 2	Case 3	Case 4	Case 5	Case 6	Case 7	Case 8
Altitude, km	77.9	75.0	71.3	66.8	60.6	53.0	47.7	43.1
Mach number	26.3	25.5	23.4	19.9	15.7	11.9	9.15	7.19
Angle of attack, deg	40.2	40.0	39.4	41.4	42.0	38.3	34.8	32.9

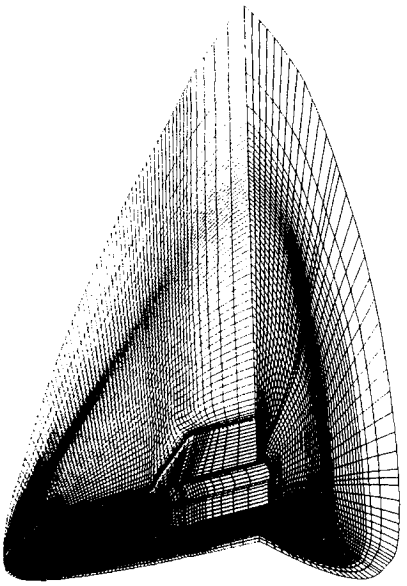

Fig. 2 Space Shuttle computational grid (86 × 69 × 66).

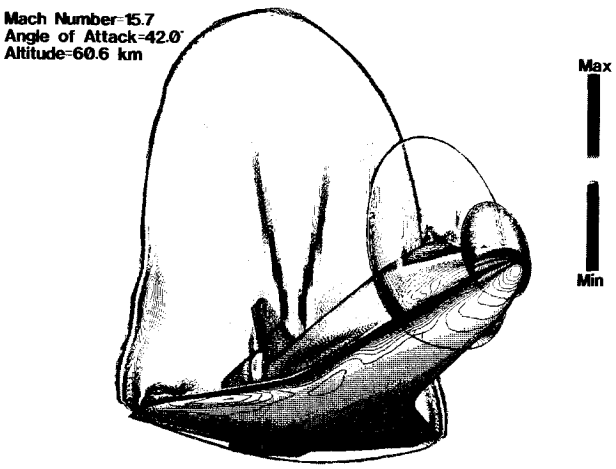

Fig. 3a Computed real-gas pressure distributions around the Space Shuttle.

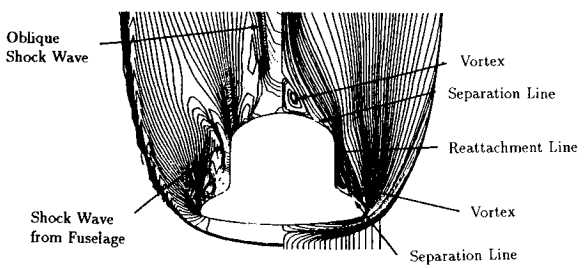

Fig. 3b Pressure distributions and two-dimensional particle traces on cross-sectional plane (X/L = 50%).

atoms are also observed at the wing tip where the temperature increases due to the interaction of shock waves. At relatively low Mach numbers, few oxygen atoms remain on the windward side, whereas at high Mach numbers, they are generated in the shock layer. The regions where oxygen molecules dissociate, are in increasing order as follows: 1) the windward shock layer; 2) the high temperature shock interaction area near the wing tip; and 3) the nose region.

Figure 7 shows the isobaric contours on a horizontal grid and the heating distribution on the windward body at an altitude of 77.9 km (M_∞ = 26.3), where the peak aerodynamic heating occurs at the nose stagnation and in the orbiter bow and wing leading-edge shock interaction region. Real-gas heat fluxes are lower than in the perfect gas, being most prominent

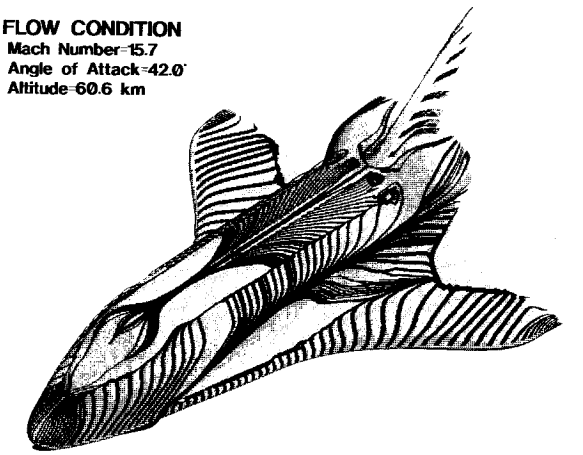

Fig. 4 Limiting streamline patterns.

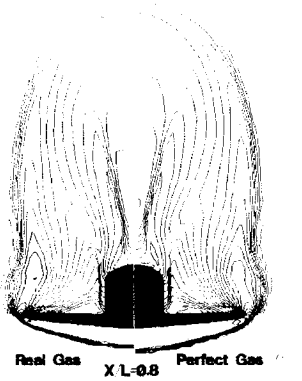

a) Alt = 53.0 km, M_∞ = 11.9

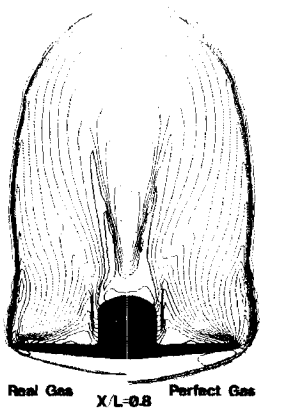

b) Alt = 60.6 km, M_∞ = 15.7

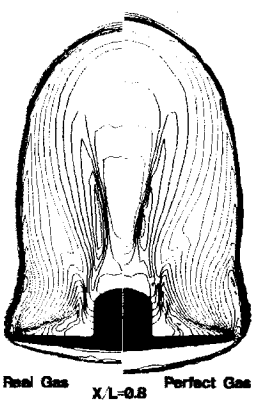

c) Alt = 77.9 km, M_∞ = 26.3

Fig. 5 Computed real/perfect distributions around the Space Shuttle.

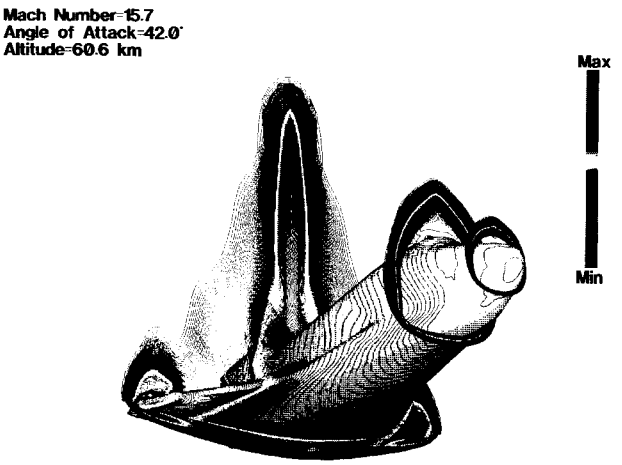

Fig. 6 Dissociated oxygen atom distributions around the Space Shuttle.

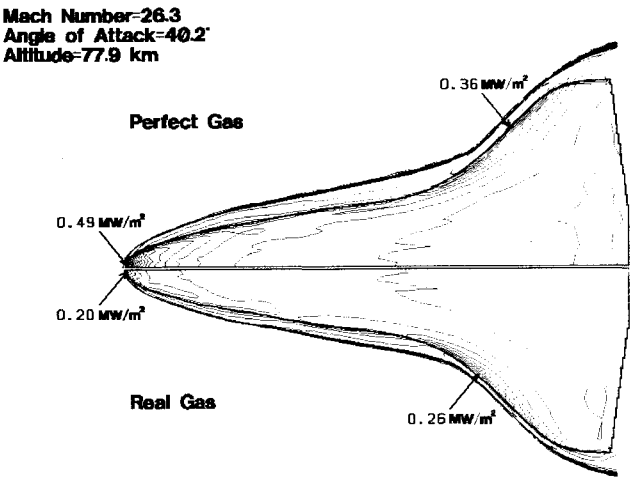

Fig. 7 Isobaric contours on a horizontal grid and the heating distributions on the windward surface by perfect/real-gas computations.

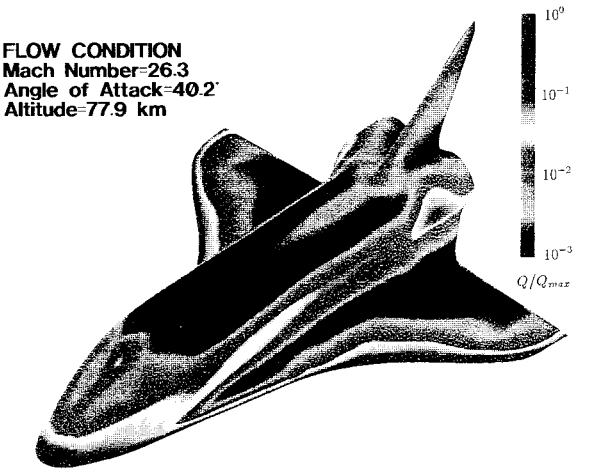

Fig. 8 Real-gas heating distributions on the leeward surface.

at the nose region; thus the wing's heating rates become higher than the nose's in the case of real gas. In every computation the bow shock wave interacts with the wing. The perfect-gas interaction occurs at almost the same place, independent of the freestream Mach number, whereas for the real gas, the location moves forward as the Mach number increases due to the shock layer's decreasing thickness. Figure 8 shows the heating distributions on the leeward surface, where vortex streak heating is observed along the reattachment line. The STS-2 orbiter was equipped with over 200 thermocouples mounted in the thermal protection system (TPS) to determine

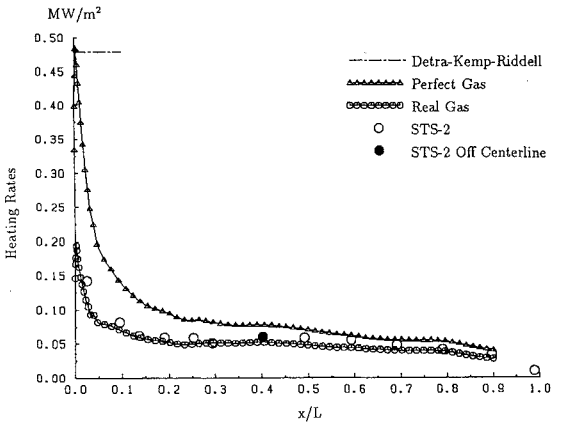

a) Alt = 77.9 km, M_∞ = 26.3

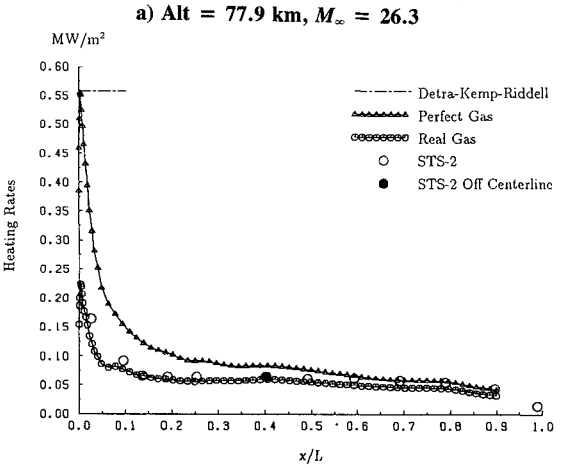

b) Alt = 75.0 km, M_∞ = 25.5

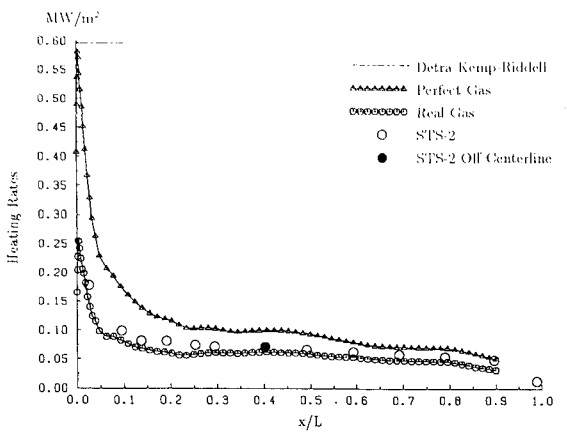

c) Alt = 71.3 km, M_∞ = 23.4

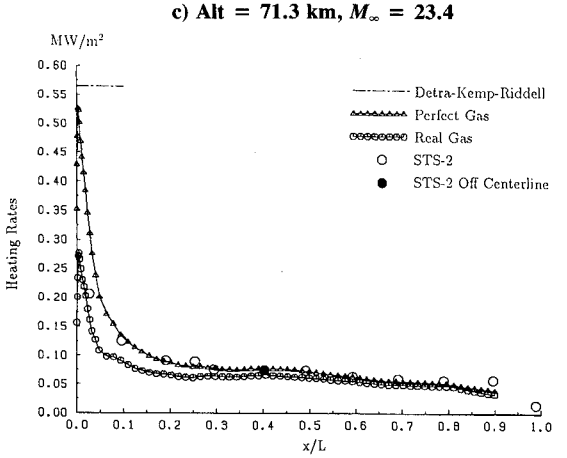

d) Alt = 66.8 km, M_∞ = 19.9

Fig. 9 Measured and predicted STS-2 heating rates on the windward centerline.

the convective heating rates.[14] The measured heating rates are compared in Fig. 9a–d with the real- and perfect-gas computational results along the windward symmetry plane at respective altitudes of 77.9, 75.0, 71.3, and 66.8 km. The calculated nose stagnation heating fluxes by the Detra-Kemp-Riddell's formula[26] are also shown. At altitudes of 77.9 and 75.0 km, the real-gas heating rates agree well with flight data, while the perfect-gas computation and Detra-Kemp-Riddell's formula overestimate by almost two times the heat fluxes from the flight data. This indicates that nonequilibrium computations are required to accurately estimate the heating rates on re-entry vehicles. In contrast, at an altitude of 67 km, the perfect-gas computation agrees with flight data. It has been previously reported that the heating rates after $x/L = 0.2$ suddenly increased at an altitude between 71–75 km, and this abrupt rise is considered to be caused by contamination of the melted acoustic sensors located at x/L stations of approximately 0.1 and 0.2.[14] Wall catalysis is a very important factor for the heating rates under high temperature environments, and more precise predictions of heating rates require the consideration of this wall catalysis.

Aerodynamic performance is also examined, i.e., the lift to drag ratio (L/D), and the location of center of pressure (X_{cp}/L_B). Figure 10 shows the computed real- and perfect-gas L/D values superimposed on both wind-tunnel preflight predictions and STS-2 flight data, with these computed values correlating well with both the flight and wind-tunnel data. In this figure there are almost no appreciable differences between the real- and perfect-gas computations, which has been also confirmed by the good prediction of the flight data by the wind-tunnel experiments. Comparisons are shown in Fig. 11 for the location of c.p. An obvious discrepancy is seen between the preflight prediction and flight data. The real flight c.p. shifted forward at high Mach numbers, thereby causing the trimmed body flap deflection to be 16 deg, whereas the predicted deflection had been only 8 deg.[1] This unexpectedly large deflection angle was necessary to fix the c.p. at the c.g. It should be noted that the differences between the wind-tunnel predictions and flight data are similar to those between the perfect- and real-gas computations throughout the entire Mach number range. Generally, as the specific heat ratio decreases, the pressure behind the shock wave increases. The low specific heat ratio is one of the high-temperature effects, thus, the real gas computations predict slightly higher pressure near the nose region. In addition, the thinner real-gas shock layer leads to a smaller shock angle, which then leads to a lower pressure on the aft windward body, causing a larger pitching moment that shifts the center of pressure forward. The perfect-gas c.p. locations slightly diverge from the preflight predictions at high Mach numbers, although at low Mach numbers (<16) good agreement is obtained. These results, however, are not disappointing when it is considered that in these computations the body flap deflection angle is fixed, and that the Space Shuttle configuration data might not be

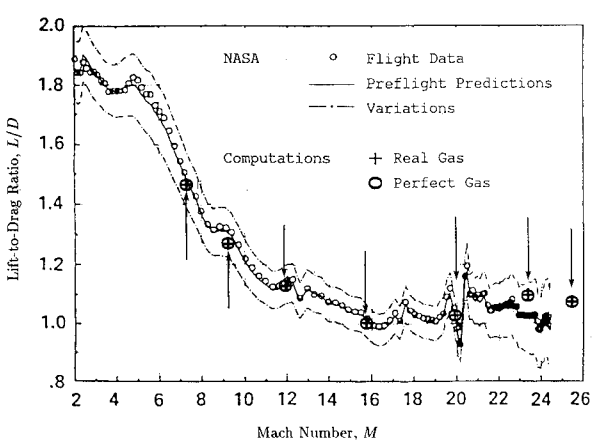

Fig. 10 STS-2 lift-to-drag ratio vs Mach number.

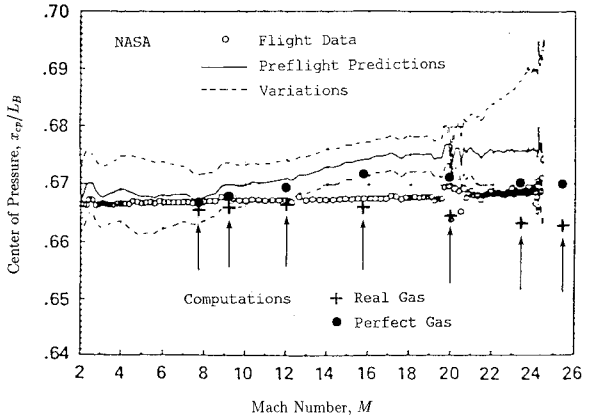

Fig. 11 STS-2 longitudinal aerodynamic center of pressure location vs Mach number.

sufficiently accurate. It can be concluded that the forward shift of the c.p. is quantitatively explained by real-gas effects, and that the high-temperature effects may also cause a very important influence on the basic aerodynamics of hypersonic vehicles.

Conclusions

Chemically reacting hypersonic flow around the Space Shuttle is computed for a series of re-entry flight conditions. A one-temperature model which takes into account 7-species finite-rate chemistry is assumed, and an implicit higher-order upwind scheme based on a generalized Roe's approximate Riemann is used. The aerodynamic characteristics and heating rates are compared with the STS-2 flight data, and a good agreement is obtained. These computations quantitatively confirm the measured forward shift of the c.p. and the reduction of heating rates due to real-gas effects. The one-temperature model, however, might overestimate the chemical reaction rates and real-gas effects near the nose stagnation at high altitudes, and further efforts will be required to improve the understanding of the physics associated with high-temperature gases.

Acknowledgments

Gratitude is extended to Tomiko Ishiguro, Satoru Ogawa, and Yoko Takakura for their encouragement, and especially to Satoru Ogawa for providing the Space Shuttle grid systems.

References

[1]Romere, P. O., Kanipe, D. B., and Young, J. C., "Space Shuttle Entry Aerodynamic Comparisons of Flight 1 with Preflight Predictions," *Journal of Spacecraft and Rockets*, Vol. 20, No. 1, 1983, pp. 15–21.

[2]Maus, J. R., Griffith, B. J., and Szema, K. Y., "Hypersonic Mach Number and Real Gas Effects on Space Shuttle Orbiter Aerodynamics," *Journal of Spacecraft and Rockets*, Vol. 21, No. 2, 1984, pp. 136–141.

[3]Chakravarthy, S. R., and Osher, S., "A New Class of High Accuracy TVD Schemes for Hyperbolic Conservation Laws," AIAA Paper 85-0363, Jan. 1985.

[4]Chakravarthy, S. R., "The Versatility and Reliability of Euler Solvers Based on High-Accuracy TVD Formulations," AIAA Paper 86-0243, Jan. 1986.

[5]Roe, P. L., "Approximate Riemann Solvers, Parameter Vectors, and Difference Schemes," *Journal of Computational Physics*, Vol. 43, No. 2, 1981, pp. 357–372.

[6]Harten, A., "High Resolution Schemes for Hyperbolic Conservation Laws," *Journal of Computational Physics*, Vol. 49, No. 3, 1983, pp. 357–393.

[7]Eberhardt, S., and Brown, K., "A Shock Capturing Technique for Hypersonic, Chemically Relaxing Flows," AIAA Paper 86-0231, Jan. 1986.

[8]Shinn, Judy L., Yee, H. C., and Uenishi, K., "Extension of a Semi-Implicit and Fully Implicit Shock-Capturing Algorithm for 3-D Fully Coupled, Chemically Reacting Flows in Generalized Coordi-

nates," AIAA Paper 87-1577, June 1987.
[9]Wada, Y., Kubota, H., Ishiguro, T., and Ogawa, S., "Fully Implicit High Resolution Scheme for Compressible Chemically Reacting Flows," *Notes on Numerical Fluid Mechanics*, Vol. 24, Vieweg, Braunsch weig, Wiesbaden, Germany, 1988, pp. 648–659.
[10]Liou, M. S., and Van Leer, B., "Splitting of Inviscid Fluxes for Real Gases," 1st National Fluid Dynamics Congress, AIAA Paper 88-3526CP, July 1988.
[11]Liu, Y., and Vinokur, M., "Nonequilibrium Flow Computations I. An Analysis of Numerical Formulations of Conservation Laws," *Journal of Computational Physics*, Vol. 83, No. 2, 1989, pp. 373–397.
[12]Wada, Y., Ogawa, S., and Ishiguro, T., "Computation of Three-Dimensional Chemically Reacting Flows around Re-Entry Vehicles," NAL SP-10, Nov. 1989, pp. 59–63.
[13]Romere, P. O., and Young, J. C., "Space Shuttle Entry Longitudinal Aerodynamic Comparisons of Flight 2 with Preflight Predictions," AIAA 12th Aerodynamic Testing Conf., AIAA Paper 82-565CP, March 1982.
[14]Zoby, E. V., "Analysis of STS-2 Experimental Heating Rates and Transition Data," *Journal of Spacecraft and Rockets*, Vol. 20, No. 3, 1983, pp. 232–237.
[15]Gnoffo, P. A., Gupta, R. N., and Shinn, J. L., "Conservation Equations and Physical Models for Hypersonic Air Flows in Thermal and Chemical Nonequilibrium," NASA TP-2867, Feb. 1989.
[16]Blottner, F. C., Johonson, M., and Ellis, M., "Chemically Reacting Viscous Flow Program for Multi-Component Gas Mixtures," Sandia Lab. Rept., SC-RR-70-754, Albuquerque, NM, Dec. 1971.
[17]Wilke, C. R., "A Viscosity Equation for Gas Mixtures, *Journal of Chemical Physics*, Vol. 18, No. 4, 1950, p. 517.
[18]Lee, J. H., "Basic Governing Equations for the Flight Regimes of Aeroassisted Orbital Transfer Vehicles," *Thermal Design of Aeroassisted Orbital Transfer Vehicles*, edited by H. F. Nelson, Vol. 96, Progress in Aeronautics and Astronautics, AIAA, New York, 1985, pp. 3–53.
[19]Candler, G. V., and MacCormack, R. W., "The Computation of Hypersonic Ionized Flows in Chemical and Thermal Nonequilibrium," AIAA Paper 88-511, Jan. 1988.
[20]Park, C., "On Convergence of Computation of Chemically Reacting Flows," AIAA Paper 85-0247, Jan. 1985.
[21]Takakura, Y., Ishiguro, T., and Ogawa, S., "On the Recent Difference Schemes for the Three-Dimensional Euler Equations," AIAA 8th CFD Conf., AIAA Paper 87-1151CP, Honolulu, HI, June 1987.
[22]Yee, H. C., "Upwind and Symmetric Shock-Capturing Scheme," NASA-TM 89464, May 1987.
[23]Peery, K. M., "Blunt-Body Flow Simulations," AIAA Paper 88-2904, July 1988.
[24]Klopfer, G. H., and Yee, H. C., "Viscous Hypersonic Shock-On-Shock Interaction on Blunt Cowl Lips," AIAA Paper 88-0233, Jan. 1988.
[25]Montagne, J. L., Yee, H. C., Klopfer, G. H., and Vinokur, M., "Hypersonic Blunt Body Computations Including Real Gas Effects," NASA TM-100074, March 1988.
[26]Detra, R. W., Kemp, N. H., and Riddell, F. R., Addendum to "Heat Transfer to Satellite Vehicles Re-Entering the Atmosphere," *Jet Propulsion*, Vol. 27, Dec. 1957, pp. 1256–1257.
[27]Ogawa, S., Ishiguro, T., and Takakura, Y., "Hyperbolic Grid Generation Scheme for Simulating Flow about Three-Dimensional Complex Configuration," *Computational Techniques and Applications: CTAC-87*, Elsevier Science, North-Holland, 1988, pp. 577–587.
[28]Rizk, Y. M., Steger, J. L., and Chaussee, D. S., "Use of Hyperbolic Grid Generation Scheme in Simulating Supersonic Viscous Flow about Three-Dimensional Winged Configurations," *Proceedings of ISCFD-Tokyo*, 1986, pp. 392–403.
[29]*Jane's All the World's Aircraft 1985–1986*, Jane's Publishing, London, 1985, pp. 497–498.